














RESEARCH ARTICLE | JULY 30 2024

## Dimensional crossover of microscopic magnetic metasurfaces for magnetic field amplification

N. Lejeune ; E. Fourneau ; A. Barrera ; O. Morris ; O. Leonard ; J. A. Arregi ; C. Navau ; V. Uhlir ; S. Bending ; A. Palau  ; A. V. Silhanek  



APL Mater. 12, 071126 (2024)

<https://doi.org/10.1063/5.0217500>



View  
Online



Export  
Citation



THE MATERIALS SCIENCE MANUFACTURER®

**Now Invent.™**



H																	He
Li	Be											B	C	N	O	F	Ne
Na	Mg											Al	Si	P	S	Cl	Ar
K	Ca	Sc	Ti	V	Cr	Mn	Fe	Co	Ni	Cu	Zn	Ga	Ge	As	Se	Br	Kr
Rb	Sr	Y	Zr	Nb	Mo	Tc	Ru	Rh	Pd	Ag	Cd	In	Sn	Sb	Te	I	Xe
Cs	Ba	La	Hf	Ta	W	Re	Os	Ir	Pt	Au	Hg	Tl	Pb	Bi	Po	At	Rn
Fr	Ra	Ac	Rf	Db	Sg	Bh	Hs	Mt	Ds	Rg	Cn	Nh	Fl	Mc	Lv	Ts	Og
Ce	Pr	Nd	Pm	Sm	Eu	Gd	Tb	Dy	Ho	Er	Tm	Yb	Lu				
Th	Pa	U	Np	Pu	Am	Cm	Bk	Cf	Es	Fm	Md	No	Lr				

American Elements  
Opens a World of Possibilities

...Now Invent!

[www.americanelements.com](http://www.americanelements.com)

© 2024 American Elements is a U.S. Registered Trademark

# Dimensional crossover of microscopic magnetic metasurfaces for magnetic field amplification

Cite as: APL Mater. 12, 071126 (2024); doi: 10.1063/5.0217500

Submitted: 5 May 2024 • Accepted: 11 July 2024 •

Published Online: 30 July 2024














View Online



Export Citation



CrossMark

N. Lejeune,<sup>1</sup>  E. Fourneau,<sup>1</sup>  A. Barrera,<sup>2</sup>  O. Morris,<sup>3</sup>  O. Leonard,<sup>3</sup>  J. A. Arregi,<sup>4</sup>  C. Navau,<sup>5</sup>   
V. Uhlíř,<sup>4,6</sup>  S. Bending,<sup>3</sup>  A. Palau,<sup>2,a)</sup>  and A. V. Silhanek<sup>1,a)</sup> 

## AFFILIATIONS

<sup>1</sup>Experimental Physics of Nanostructured Materials, Department of Physics, Université de Liège, Sart Tilman, B-4000 Liège, Belgium

<sup>2</sup>Institut de Ciència de Materials de Barcelona, ICMA-B-CSIC, Campus de la UAB, 08193 Bellaterra, Spain

<sup>3</sup>Centre for Nanoscience and Nanotechnology, Department of Physics, University of Bath, Bath BA2 7AY, United Kingdom

<sup>4</sup>CEITEC BUT, Brno University of Technology, Purkyňova 123, 612 00 Brno, Czech Republic

<sup>5</sup>Grup d'Electromagnetisme, Departament de Física, Universitat Autònoma de Barcelona, 08193, Bellaterra, Barcelona, Spain

<sup>6</sup>Institute of Physical Engineering, Brno University of Technology, Technická 2, 616 69 Brno, Czechia

<sup>a)</sup>Authors to whom correspondence should be addressed: [palau@icmab.es](mailto:palau@icmab.es) and [asilhanek@uliege.be](mailto:asilhanek@uliege.be)

## ABSTRACT

Transformation optics applied to low frequency magnetic systems have been recently implemented to design magnetic field concentrators and cloaks with superior performance. Although this achievement has been amply demonstrated theoretically and experimentally in bulk 3D macrostructures, the performance of these devices at low dimensions remains an open question. In this work, we numerically investigate the non-monotonic evolution of the gain of a magnetic metamaterial field concentrator as the axial dimension is progressively shrunk. In particular, we show that in planar structures, the role played by the diamagnetic components becomes negligible, whereas the paramagnetic elements increase their magnetic field channeling efficiency. This is further demonstrated experimentally by tracking the gain of superconductor-ferromagnet concentrators through the superconducting transition. Interestingly, for thicknesses where the diamagnetic petals play an important role in the concentration gain, they also help to reduce the stray field of the concentrator, thus limiting the perturbation of the external field (invisibility). Our findings establish a roadmap and set clear geometrical limits for designing low dimensional magnetic field concentrators.

© 2024 Author(s). All article content, except where otherwise noted, is licensed under a Creative Commons Attribution (CC BY) license (<https://creativecommons.org/licenses/by/4.0/>). <https://doi.org/10.1063/5.0217500>

## I. INTRODUCTION

Magnetic field concentrators (MFCs) are structures designed to channel and enhance the strength of magnetic fields. They work by guiding the magnetic field lines through a specific path, thereby increasing the magnetic field density in a targeted region. These devices play a vital role in enhancing the sensitivity and efficiency of magnetic sensors and are engineered to manipulate and harness magnetic fields in a way that may serve specific technological needs, such as monitoring power transmission cables,<sup>1</sup> magnetoencephalography,<sup>2</sup> magnetoresistance biosensors,<sup>3,4</sup> and magnetometry based on nitrogen-vacancy quantum probes.<sup>4-6</sup> The essential

parameters determining the performance of MFC are the material choice and the imposed geometry.<sup>7-9</sup> Although the vast majority of MFC is based on soft ferromagnetic (FM) alloys, some high field applications have been proposed based on the flux-focusing produced between neighboring superconducting parts.<sup>10</sup>

The advent of transformation optics<sup>11</sup> brought about a paradigm shift in the way scientists approach, understand, and conceive magnetic field concentrators. This discipline involves a coordinate transformation to control light paths within media. Since Maxwell's equations are form-invariant to coordinate transformations, only the components of the permittivity tensor and the permeability tensor are affected by the transformation. This approach

has served as a bridge between theoretical physics and practical engineering, providing a platform to design electromagnetic devices with unprecedented functionalities and efficiencies.<sup>12</sup> In the limit of very low frequencies, where the electric and magnetic fields become separable in Maxwell's equations,<sup>13</sup> the fundamental ingredient needed to achieve efficient guidance of magnetic field lines and negligible external distortion of a uniformly applied field is a highly anisotropic magnetic permeability tensor  $\mu$ .<sup>14</sup>

More precisely, this condition can be fulfilled in an axially symmetric structure by combining radial ( $\mu_r$ ) and angular ( $\mu_\theta$ ) relative permeability components fulfilling the relations  $\mu_r\mu_\theta = 1$  and  $\mu_r \gg \mu_\theta$ .<sup>14</sup> Recognizing that natural materials do not exist that satisfy these conditions, scientists have proposed several metamaterials, constructed from alternating layers or wedges, to serve as approximations. These materials strategically combine wedges of superconductors to suppress azimuthal permeability and ferromagnetic wedges to enhance  $\mu_r$  and, thus, tailor their effective permeabilities to enable the desired electromagnetic behavior. It has been theoretically and experimentally shown that a long cylindrical shell made of such a metamaterial with inner and outer radii of  $R_i$  and  $R_o$ , respectively, is able to enhance the magnetic field in the sensing area by a factor of  $R_o/R_i$ .<sup>15–17</sup> Similar structures combining ferromagnetic and conducting materials have even shown potential for concentrating alternating magnetic fields.<sup>18</sup>

The continuous strive for high density and on-chip integrated devices working at room temperature has motivated the investigation of downscaling the metamaterial shells to realize planar meso/micro-metasurfaces made of only magnetic materials.<sup>19</sup> In this context, it has been shown that the concentration power depends on the thickness of the device and achieves optimal performance when the thickness is about twice the inner radius of the MFC.<sup>19</sup> In addition, the presence of magnetic domains, the irreversible magnetic response, and the saturation of the MFC have been shown to have a detrimental impact on the performance of the concentrator by reducing the range of magnetic fields over which the device can operate.<sup>19</sup> To date, it remains unclear whether it is possible to further enhance the gain of 2D magnetic concentrators by inserting highly diamagnetic petals, similar to the successful strategy already demonstrated for 3D devices.<sup>16</sup>

In this work, we address this question by numerically investigating the effect of diamagnetic petals sandwiched between neighboring paramagnetic petals on devices spanning the whole range of possible thicknesses. For MFC with thicknesses larger than the outer radius ( $t > R_o$ ), the presence of diamagnetic petals gives rise to more than 100% enhancement of the concentration gain. By reducing their thickness, the paramagnetic petals become more efficient by collecting additional magnetic field lines from the top and bottom surfaces, although the overall gain of the device decreases due to the underperformance of the diamagnetic petals. For thicknesses smaller than the internal radius ( $t < R_i$ ), the diamagnetic petals play a negligible role in the concentration factor and could be simply omitted. We have experimentally confirmed this thin film limit for microscale planar concentrators made of a soft ferromagnet (Permalloy) combined with superconducting petals made of a high temperature superconductor (YBa<sub>2</sub>Cu<sub>3</sub>O<sub>7</sub>). We have also demonstrated that adding a magnetic disk with a slit in the core of the concentrator leads to a boost in the concentration effect. In the

thickness regime where the diamagnetic petals boost the gain of the structures, they also promote the invisibility of MFC.

## II. RESULTS AND DISCUSSION

### A. Finite element modeling

The MFC under consideration follows the design proposed in Ref. 16 and consists of a shell with an inner radius of  $R_i = 100 \mu\text{m}$  and an outer radius of  $R_o = 400 \mu\text{m}$  with alternating ideal paramagnetic and diamagnetic petals, as schematically shown in the inset of Fig. 1(a). In this model, the ideal paramagnetic material has an exceptionally high permeability and no saturation magnetization. This behavior corresponds to the magnetic response of a soft ferromagnetic material, such as Permalloy, in a linear regime, specifically at low applied external fields. Conversely, the ideal diamagnetic material is described by a superconductor in the Meissner state with a critical temperature of  $T_c$ . In this context, we can directly compare the response of the MFC with diamagnetic petals ( $T < T_c$ ) and that of the same concentrator without diamagnetic petals ( $T > T_c$ ). Note that the assumption of the superconductor as a perfect screening component represents an upper bound on the size of any effects. In films with a thickness comparable to or smaller than the superconducting penetration depth, the field will be able to penetrate from top to bottom. Hence, any screening of the in-plane field is going to be substantially less than this in reality.

Simulations are conducted using the finite element method, with the system discretized into a tetrahedral mesh grid. The stationary Maxwell's equations in the absence of charge currents are solved using the magnetostatic module of Comsol Multiphysics software, with a relative accuracy set to  $10^{-5}$ . The boundary condition dictates that the local magnetic field  $\mathbf{B}$  equals the applied field  $\mathbf{B}_a$  on each boundary of the simulation box. The dimensions of these faces are sufficiently large to ensure that the error in gain resulting from field line confinement remains below 1%. The relative permeability values for the ideal paramagnetic and diamagnetic materials are specified as  $10^5$  and  $10^{-5}$ , respectively. These values have been chosen in such a way that the radial and angular magnetic permeabilities,  $\mu_r$  and  $\mu_\theta$ , satisfy the relation  $\mu_r\mu_\theta = 1$  necessary for avoiding perturbations of the magnetic field around the device.<sup>20</sup>

Figure 1(a) shows the concentration gain  $G = \frac{\mathbf{B}_0 \cdot \mathbf{B}_c}{|\mathbf{B}_a|^2}$ , with  $\mathbf{B}_0$  being the field at the inversion symmetry point of the structure (i.e., its center), as a function of thickness. The red (blue) data points correspond to the device without (with) diamagnetic petals. The dotted lines indicate the associated asymptotic limits for an infinite cylindrical sample, as calculated in Ref. 20. For  $t > 10^4 \mu\text{m}$  (i.e.,  $t/R_i > 100$ ), the response is nearly that of an infinite cylindrical device. For the MFC with only paramagnetic petals, as  $t$  decreases,  $G$  increases. The reason for this effect is that the additional magnetic field lines entering through the upper and lower surfaces of the paramagnetic petals, aligned with the applied field, further contribute to the gain. In striking contrast to this, for the MFC with diamagnetic petals,  $G$  decreases as  $t$  decreases. This behavior results from the fact that for thin structures ( $t/w < 1$ , with  $w$  being the average width of the petal), the expulsion of field lines by the diamagnetic petals at the top and bottom surfaces involves very little lateral displacement parallel to the sample plane and is hence rather ineffective at screening the magnetic field from these regions and imposing the required

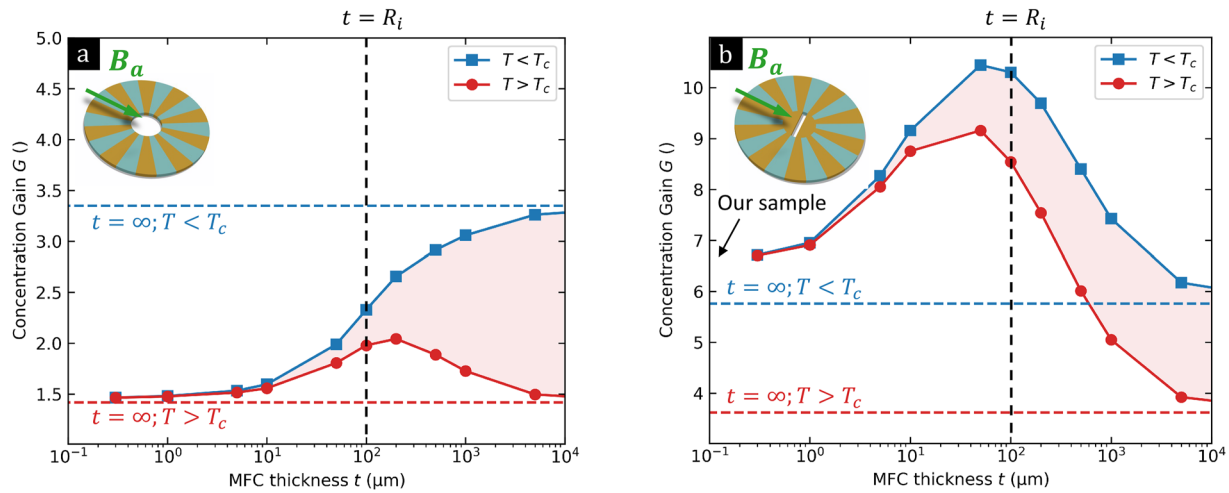


**FIG. 1.** Simulation of the variation in concentration gain with the MFC thickness for concentrators of outer radius  $R_o = 400 \mu\text{m}$  and inner radius  $R_i = 100 \mu\text{m}$ . The simulation is repeated with diamagnetic petals having a relative permeability  $\mu_r$  of both 1 and  $10^{-5}$  to mimic superconducting petals above and below their critical temperature,  $T_c$ . Panels (a) and (b) illustrate the differences in results obtained with an MFC, with panel (a) featuring an MFC without a central core and panel (b) depicting results with a ferromagnetic (FM) core.

condition on the anisotropic permeability. Note that the performance increase in the paramagnetic petals does not compensate for the underperformance of the diamagnetic petals, and an overall decrease in gain is observed as the thickness decreases. For the MFC with only paramagnetic petals, an optimum gain is observed when  $t/R_i \sim 2$ . Below this ratio, the stray field at the tip of the petals rapidly fans out, leading to a net decrease in the gain. It is worth noting that for  $t < 10 \mu\text{m}$ , the presence of diamagnetic petals becomes irrelevant for this geometry.

In an attempt to reach higher values of concentration, we investigate the response of a similar device in which we have filled the inner core with a paramagnetic material with a  $20 \mu\text{m}$  wide slit [see inset in Fig. 1(b)]. The results for an in-plane applied field perpendicular to the slit are presented in Fig. 1(b). The thickness

dependence of the gain for this MFC follows a similar trend to that of the empty-core MFC, but with a more pronounced enhancement at intermediate thicknesses. Although the diamagnetic petals seem to contribute to a larger range of thicknesses, their role eventually becomes negligible for  $t < 5 \mu\text{m}$ .

Another intriguing property of flower-like magnetic metamaterial concentrators, which has been theoretically predicted and experimentally demonstrated for macroscopic structures, is the confinement of the stray field in the close vicinity of the concentrator, rendering it magnetically invisible. In other words, for perfectly invisible concentrators, the magnetic field around the MFC exactly matches the applied field.<sup>20</sup> In Fig. 2, we simulate the impact of the MFC on the magnetic field landscape, taking into account the thickness of an eight-petal-concentrator. To assess the magnetic

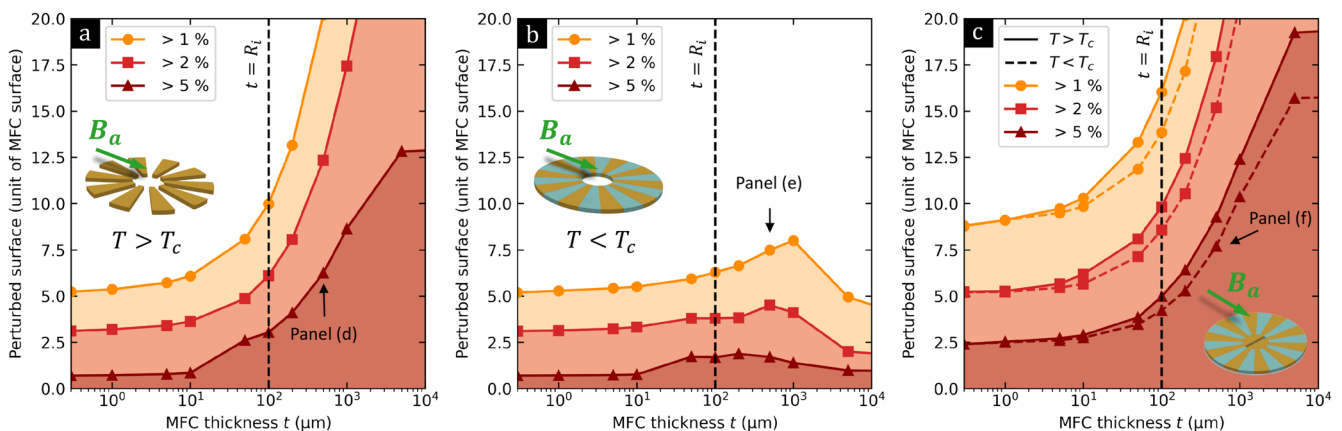


**FIG. 2.** Magnetic field perturbation  $|\mathbf{B} - \mathbf{B}_a|/B_a$  (%) as a function of the MFC thickness. Evolution of the footprint area in the vicinity of the MFC for which the perturbation is larger than 5%, 2%, and 1% (a) for a MFC without FM core above  $T_c$ , (b) without core below  $T_c$ , and (c) in the presence of a FM core below and above  $T_c$ . (d)–(f) Top and side views of the perturbation areas calculated for  $500\text{-}\mu\text{m}$ -thick devices.

05 August 2024 11:33:52

invisibility, we calculate the projected area around the MFC within which the local magnetic field deviates by no more than a few percent of the applied field, i.e.,  $\varepsilon = \frac{|B - B_0|}{B_0} < 1, 2, 5\%$ .

In the regime above the critical temperature of the device [Fig. 2(a)], the area affected by the MFC increases linearly with the sample thickness (the abscissa is expressed on a logarithmic scale). For instance, the 1% perturbation region covers a surface that grows from five times the concentrator's surface when  $t = 1 \mu\text{m}$  to more than 20 times for 0.5-mm-thick samples. For the sake of clarity, the perturbed area for the specific case of  $t = 500 \mu\text{m}$  is displayed in panel (d) for both an in-plane (IP) and an out-of-plane (OOP) cross-sectional view. Both cuts are symmetry planes of the device, as shown in the inset of panel (e).

When  $T < T_c$  [Fig. 2(b)], the presence of the diamagnetic petals drastically reduces the extent of the stray field, which remains confined within a radial distance of  $2R_i$  from the edge of the MFC. Note that a shallow maximum of the perturbed fields outside the MFC develops when  $t$  is about  $2R_o$ . The improved invisibility of the MFC with diamagnetic petals becomes more apparent by comparing panels (d) and (e), corresponding to the absence and presence of diamagnetic petals, respectively. However, it should be noted that, similar to the gain improvement shown in Fig. 1, a negligible difference is observed when the thickness of the device falls below  $t = 10 \mu\text{m}$ . Finally, for the concentrator with a ferromagnetic core [panels (c) and (f)], the difference between having (circles connected by dashed lines) or not having (squares connected by lines) diamagnetic petals remains negligible even for the thicker samples.

These results suggest that diamagnetic petals have little influence on the gain of thin MFC but may offer the beneficial effect of boosting the concentration gain and improving their invisibility for thick devices, thus reducing their influence on neighboring electromagnetic components of the chip. In Sec. II B, we address these aspects from an experimental point of view.

## B. Experimental results

The theoretical predictions for an infinitely long cylindrical MFC based on a model of combined ideal paramagnetic and diamagnetic components were experimentally validated in Ref. 16. Here, we will explore the opposite extreme and gauge the impact

of implementing diamagnetic elements in planar 2D on-chip MFC. To this end, we have fabricated sub-millimeter MFC alternating Permalloy (Py,  $\text{Ni}_{80}\text{Fe}_{20}$ ) petals with superconducting petals made of a high-temperature superconductor,  $\text{YBa}_2\text{Cu}_3\text{O}_{7-\delta}$  (YBCO). The choice of YBCO is well justified by the fact that a strong diamagnetic response is expected due to its high lower critical field for IP magnetic fields ( $\mu_0 H_{c1} \approx 23 \text{ mT}$ ),<sup>21,22</sup> and at the same time, its high critical temperature ( $T_c \approx 87 \text{ K}$ ) offers a wide and easily accessible temperature range for exploring different diamagnetic regimes. The simulations are applicable in the region where the magnetization is proportional to the applied magnetic field, i.e., for  $H$  below the saturation field  $H_s \approx 1 \text{ mT}$  of the Py (see the [supplementary material](#)). Note that this field is substantially lower than the  $H_{c1}$  of YBCO.

Five different devices having an external radius  $R_o = 400 \mu\text{m}$  and petals touching a central Py disk of  $R_i = 100 \mu\text{m}$  were fabricated by growing a 100 nm-thick YBCO film on a  $5 \times 5 \text{ mm}^2$  (001)- $\text{LaAlO}_3$  (LAO) substrate by pulsed laser deposition at  $800^\circ\text{C}$  under an  $\text{O}_2$  partial pressure of 0.3 mbar. The YBCO petals were then defined by standard photolithography and wet etching. Subsequently, the Py parts were fabricated by DC magnetron sputtering and lift-off. The Py petals have been grown with a slight overlap on the YBCO petals to ensure there is no gap between the two materials and, thus, maximize the magnetic channeling effect. An optical image depicting one of the devices is shown in Fig. 3(a). The thickness of the YBCO and Py layers is 100 nm, thus avoiding the formation of stripe domains in the Py film.<sup>23,24</sup> All devices have a slit-shaped gap of width  $g$  in the center, allowing us to pick up the OOP components of the stray field [as schematically represented in Fig. 3(b)], which is proportional to the magnetic field concentration gain. A device with no superconducting components and  $g = 5 \mu\text{m}$  is used as a reference. Four other devices, two of them with 16 petals (half superconducting, half ferromagnetic) and gaps of 5 and  $20 \mu\text{m}$ , and another two with four petals (half superconducting, half ferromagnetic) and gaps of 5 and  $20 \mu\text{m}$ , were investigated, and all exhibit similar behavior.

The MFC was investigated through quantitative magneto-optical imaging (MOI) based on the Faraday rotation of an indicator film placed on top of the device. Details of the technique and the setup can be found in Ref. 25. In order to investigate the possible reduction of the critical temperature of the superconducting components after microstructuring, we cooled down the sample to the

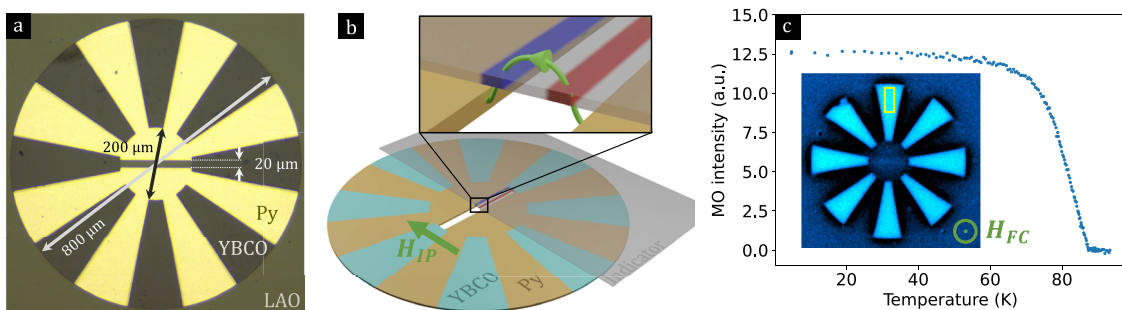


**FIG. 3.** (a) Optical image of the investigated sample. The outer radius is four times larger than the inner one. (b) Schematic view of the experimental setup used to extract the polarization at the gap via magneto-optical imaging (MOI). A Faraday indicator is placed on top of the sample mounted in a cryostat, and the in-plane magnetic field is swept while capturing images of the magnetic landscape at various temperatures. The indicator senses the out-of-plane component of the magnetic field coming from the stray field above the gap, as depicted in the close-up view. (c) Evolution of the MOI signal arising from trapped flux in the YBCO after field cooling in an out-of-plane field as a function of temperature. The mean value in the yellow rectangle from which the slightly temperature-dependent background was subtracted gradually drops to zero at  $T_c = 87 \text{ K}$ .

base temperature of our cryostat ( $\sim 4$  K) while applying an OOP magnetic field  $\mu_0 H_{FC} = 4$  mT; subsequently, the field was turned off and the trapped flux was monitored as a function of temperature. Figure 3(c) shows the background subtracted intensity recorded in the rectangular box indicated in the inset as a function of temperature. A superconducting critical temperature  $T_c \approx 87$  K is obtained for all superconducting petals. The obtained sequence of images as a function of temperature shows that the magnetic response of the superconducting petals is uniform throughout the entire device (see animation in the [supplementary material](#)).

The investigation of the MFC exposed to an IP field requires a very specific image post-processing protocol. Indeed, in view of the fact that the FM elements exhibit a remnant magnetization, standard image processing involving background subtraction would require one to heat up beyond the Curie temperature of Py ( $\sim 350^\circ\text{C}$ ). Here, we introduce an alternative method consisting of averaging the magnetic images corresponding to the two opposite polarities of the maximum IP applied magnetic field,  $\pm\mu_0 H_{\text{max}} = 1.95$  mT. By doing so, the stray field emanating from the FM cancels out, and only the illumination background remains. The result can then be subtracted from the acquired images to reveal the stray field of the sample.

The OOP component of the stray field in the gap region can then be recorded as a function of the applied IP field and temperature, as shown in Fig. 4(a). By computing the mean intensity value in regions 1 and 2, indicated by the yellow frame

in picture (d) of Fig. 4, the hysteresis loop shown in panel (a) is obtained as the IP field is cycled. Note that the magnetically active indicator has a nearly linear response to OOP fields up to 125 mT (well above the maximum stray field  $\sim 10$  mT), ensuring good proportionality between light intensity and the OOP component of the stray field. As temperature decreases, both the saturation polarization [green circles in panel (c)] and the coercive field [green triangles in panel (d)] increase, in agreement with previous reports on Py films.<sup>26,27</sup> Note, however, that no particular feature or behavior is observed when the YBCO switches from a non-magnetic ( $T = 100$  K  $> T_c$ ) to a strongly diamagnetic ( $T = 80$  K  $< T_c$ ) state. More precisely, the superconducting transition in the YBCO elements does not seem to induce an enhancement of the magnetic field concentration efficiency. Further measurements comparing a MFC with and without diamagnetic petals corroborate this result. These findings are consistent with the results of finite-element simulations presented in Fig. 1(b), showing that for the maximum IP applied field (2 mT), the difference between having and not having perfectly diamagnetic petals is about  $1 \mu\text{T}$ , well below our experimental resolution.

Note that the hysteresis loop in Fig. 4(a) is not centered at  $\mu_0 H = 0$ , but it is biased to negative fields. This behavior arises due to the fact that the maximum applied IP field is not enough to completely saturate the magnetic moment of the MFC. The noisy response in the vicinity of  $\mu_0 H = 0$  results from the inevitable formation of magnetic domains in the indicator used to capture the MOI images. The

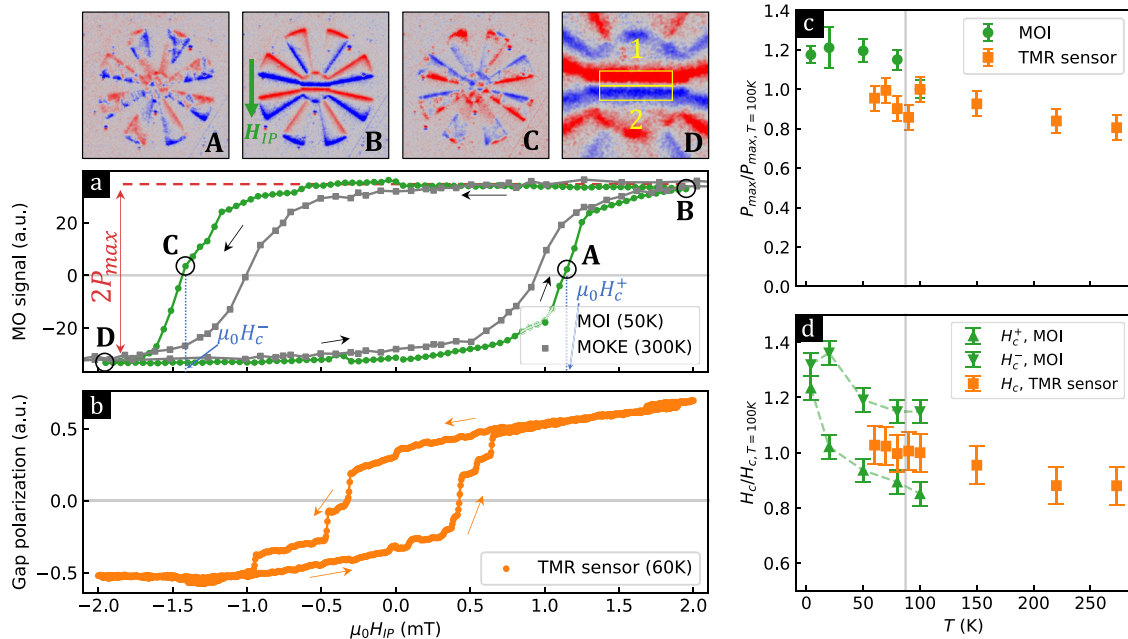


**FIG. 4.** (a) Representative hysteresis curve of the OOP component of the stray field at the gap at  $T = 50$  K, extracted from MOI sweeps (green circles). The gap polarization  $P$  is defined as the difference in the mean pixel value between region 2 and region 1, both shown in image (d). MOI images at different magnetic fields close to saturation or polarization reversal are shown in panels (a)–(d). The hysteresis loop starts at 0 mT in the negative remnant configuration, and the field is swept in plane. Gray square symbols show the hysteresis loop obtained on the same sample by tracking the longitudinal magnetic Kerr signal at room temperature and sweeping the magnetic field between  $-8$  and  $+8$  mT. The result is shown for an in-plane field ranging from  $-2$  to  $+2$  mT, as the device is at saturation outside that range. (b) Magnetic hysteresis loop at  $T = 60$  K measured with a TMR sensor at the edge of the slot in an eight-petal Py/YBCO concentrator (see the text). (c) Relative evolution of the maximum polarization with temperature for both MOI and scanning TMR sensor techniques. The maximum polarization is defined as half the difference between polarization at maximum and minimum fields. (d) Temperature dependence of the normalized in-plane coercive field at which the magnetic polarization reverses. For MOI, both field directions are differentiated. The dashed lines are guides to the eye, and the vertical gray line is at  $T_c \approx 87$  K.

MOI images corresponding to points (a)–(d) in panel (a) show the OOP component of the stray field and reveal the proliferation of magnetic domains at the coercive field.

Further information concerning the magnetic response of the MFC has been obtained through two complementary techniques. First, magneto-optical Kerr effect (MOKE) microscopy allowed for tracking the evolution of the IP magnetic domains in the FM petals at room temperature. We use a commercial MOKE microscope from Evico magnetics in the longitudinal Kerr configuration using 20× and 10× magnification objectives.<sup>28</sup> The MOKE images presented in this work were obtained by employing background subtraction. A snapshot of the magnetic domains near the coercive field of the structure is presented in Annex I, and an animation of the MOKE images as a function of the field can be found in the [supplementary material](#). By computing the average intensity signal of the entire device, it is possible to obtain a hysteresis loop, as shown by the gray square symbols in Fig. 4(a). The lower coercivity of this loop with respect to that obtained by MOI results from the temperature dependence of the  $\mu_0 H_c$ , as shown in panel (d). Second, we compare it to low-temperature scanning tunnel magnetoresistance (TMR) microscopy, which is a non-invasive technique permitting one to either scan an area to reveal the OOP magnetic landscape or acquire the local response by parking the sensor in a particular spot. A local hysteresis loop is presented in Fig. 4(b), and scan areas are available in Annex I. Note that the magnetization loop obtained by this method exhibits substantially smaller coercivity. This difference might be attributed to the fact that the coercive field is position dependent, as revealed by the MOKE measurements presented in Annex I. The staircase shape of the TMR loop shown in Fig. 4(a) can be naturally explained by the process of depinning and reversing adjacent magnetic domains. Annex II summarizes the hysteresis loops obtained by TMR measurements for several devices and as a function of temperature.

It is worth pointing out that interface effects between the superconducting and ferromagnetic components<sup>29–32</sup> can be neglected in the analysis of the magnetic response of the system in view of the fact that they represent merely 0.1% of the total surface of the device. Since YBCO and Py are not grown in the same chamber, we do not expect a high-quality interface between these two materials. More transparent interfaces will likely enhance the inverse proximity effect and reduce the superconducting properties of a thin layer, which could actually result in a device performance reduction.

### III. CONCLUSIONS

We have numerically investigated the performance of magnetic field concentrators based on cylindrical metamaterial shell structures as a function of their thickness for fixed inner and outer radii. Two figures of merit are introduced to evaluate the performance of the devices: the gain and the invisibility. For MFC without diamagnetic petals, the gain is optimized when the thickness is comparable to the inner radius of the shell. This maximum arises from the competition between the increased dispersion of the stray field emanating from the tips of the petals as the thickness decreases and the enhancement of the collected field lines through the upper and lower surfaces as the thickness decreases. We show that the effect of the diamagnetic petals on the gain rapidly becomes negligible as the thickness decreases, but they play an important role in

limiting the perturbation of the field outside the structure. We have experimentally investigated the thin-film limit in devices composed of alternating superconducting and ferromagnetic petals and confirmed the predictions of the numerical model. The obtained results provide clear guidelines for designing low dimensional magnetic field concentrators.

### SUPPLEMENTARY MATERIAL

Additional hysteresis loops measured in different locations close to the gap using both MOKE microscopy and scanning TMR can be found in the [supplementary material](#). In addition, we show animations of the MOI and MOKE sweeps.

### ACKNOWLEDGMENTS

This work was supported by the Fonds de la Recherche Scientifique - FNRS under the program Grant Nos. PDR T.0204.21 and CDR J.0176.22, EraNet-CHISTERA Grant No. R.8003.21, the Spanish Ministry of Science and Innovation MCIN/AEI/10.13039/501100011033/through CHIST-ERA Grant Nos. PCI2021-122028-2A and PCI2021-122083-2A cofinanced by the European Union Next Generation EU/PRTR, HTSUPERFUN Grant No. PID2021-124680OB-I00 cofinanced by ERDF as a way of making Europe, MAGNETOLIGHT TED2021-130402B-I00, “Severo Ochoa” Programme CEX2023-001263-S and PID2019-104670GB-I00 of the Agencia Estatal de Investigación/Fondo Europeo de Desarrollo Regional (UE), and by COST (European Cooperation in Science and Technology) [[www.cost.eu](http://www.cost.eu)] through COST Action Grant No. SUPERQUMAP (CA 21144). Access to the CEITEC Nano Research Infrastructure was supported by the Ministry of Education, Youth, and Sports (MEYS) of the Czech Republic under Project No. Czech NanoLab (LM2023051). J.A.A. and V.U. acknowledge the support from the TACR EraNet CHIST-ERA Project No. MetaMagIC TH77010001. S. J. B. was supported by the Engineering and Physical Sciences Research Council (EPSRC) in the United Kingdom under Grant No. EP/W022680/1. N. L. acknowledges the support from FRS-FNRS (Research Fellowships FRIA). The work of E. Fourneau has been financially supported by the FWO and F.R.S.-FNRS under the Excellence of Science (EOS) Project No. O.0028.22.

### AUTHOR DECLARATIONS

#### Conflict of Interest

The authors have no conflicts to disclose.

#### Author Contributions

N. L. and E. F. contributed equally to this work.

**N. Lejeune:** Data curation (equal); Formal analysis (equal); Investigation (equal); Validation (equal); Visualization (lead); Writing – original draft (supporting); Writing – review & editing (equal).  
**E. Fourneau:** Data curation (equal); Formal analysis (equal); Investigation (equal); Validation (equal); Visualization (lead); Writing – original draft (equal); Writing – review & editing (equal).

**A. Barrera:** Resources (equal); Writing – review & editing (equal). **O. Morris:** Data curation (equal); Formal analysis (equal); Investigation (equal); Validation (equal); Writing – review & editing (equal). **O. Leonard:** Data curation (equal); Formal analysis (equal); Investigation (equal); Validation (equal); Writing – review & editing (equal). **J. A. Arregi:** Data curation (equal); Formal analysis (equal); Validation (equal); Visualization (supporting); Writing – review & editing (equal). **C. Navau:** Conceptualization (equal); Funding acquisition (equal); Project administration (equal); Supervision (equal); Writing – review & editing (equal). **V. Uhlir:** Conceptualization (equal); Funding acquisition (equal); Project administration (equal); Supervision (equal); Writing – review & editing (equal). **S. Bending:** Conceptualization (equal); Formal analysis (equal); Funding acquisition (equal); Project administration (equal); Supervision (equal); Writing – review & editing (equal). **A. Palau:** Conceptualization (equal); Funding acquisition (equal); Project administration (equal); Resources (lead); Supervision (equal); Writing – review & editing (equal). **A. V. Silhanek:** Conceptualization (equal); Formal analysis (supporting); Project administration (equal); Supervision (equal); Visualization (supporting); Writing – original draft (lead); Writing – review & editing (lead).

## DATA AVAILABILITY

The data that support the findings of this study are available from the corresponding authors upon reasonable request.

## REFERENCES

- K. Zhu and P. W. T. Pong, “Curved trapezoidal magnetic flux concentrator design for current measurement of multi-core power cable with magnetic sensing,” *IEEE Trans. Magn.* **55**, 4001809 (2019).
- A. Kanno, N. Nakasato, M. Oogane, K. Fujiwara, T. Nakano, T. Arimoto, H. Matsuzaki, and Y. Ando, “Scalp attached tangential magnetoencephalography using tunnel magneto-resistive sensors,” *Sci. Rep.* **12**, 6106 (2022).
- C. Dey, P. Yari, and K. Wu, “Recent advances in magnetoresistance biosensors: A short review,” *Nano Futures* **7**, 012002 (2023).
- Y. Chen, Q. Lin, H. Cheng, H. Huang, J. Shao, Y. Ye, G.-S. Liu, L. Chen, Y. Luo, and Z. Chen, “Nanodiamond-based optical-fiber quantum probe for magnetic field and biological sensing,” *ACS Sens.* **7**, 3660 (2022).
- I. Fescenko, A. Jarmola, I. Savukov, P. Kehayias, J. Smits, J. Damron, N. Ristoff, N. Mosavian, and V. M. Acosta, “Diamond magnetometer enhanced by ferrite flux concentrators,” *Phys. Rev. Res.* **2**, 023394 (2020).
- X. Mao, K. Huang, G. Ran, Q. Huang, S. Qu, X. He, Q. Hu, and Z. Lin, “An integrated magnetometer module with MFCs based on diamond NV centers,” *IEEE Sens. J.* **23**, 16161–16167 (2023).
- P. M. Drljača, F. Vincent, P.-A. Besse, and R. S. Popović, “Design of planar magnetic concentrators for high sensitivity Hall devices,” *Sens. Actuators, A* **97–98**, 10–14 (2002).
- X. Sun, L. Jiang, and P. W. Pong, “Magnetic flux concentration at micrometer scale,” *Microelectron. Eng.* **111**, 77–81 (2013).
- X. Zhang, Y. Bi, G. Chen, J. Liu, J. Li, K. Feng, C. Lv, and W. Wang, “Influence of size parameters and magnetic field intensity upon the amplification characteristics of magnetic flux concentrators,” *AIP Adv.* **8**, 125222 (2018).
- T. Kiyoshi, S. Choi, S. Matsumoto, T. Asano, and D. Uglietti, “Magnetic flux concentrator using Gd-Ba-Cu-O bulk superconductors,” *IEEE Trans. Appl. Supercond.* **19**, 2174 (2009).
- J. B. Pendry, D. Schurig, and D. R. Smith, “Controlling electromagnetic fields,” *Science* **312**, 1780–1782 (2006).
- D. Schurig, J. J. Mock, B. J. Justice, S. A. Cummer, J. B. Pendry, A. F. Starr, and D. R. Smith, “Metamaterial electromagnetic cloak at microwave frequencies,” *Science* **314**, 977–980 (2006).
- B. Wood and J. B. Pendry, “Metamaterials at zero frequency,” *J. Phys.: Condens. Matter* **19**, 076208 (2007).
- A. Sanchez, C. Navau, J. Prat-Camps, and D.-X. Chen, “Antimagnets: Controlling magnetic fields with superconductor–metamaterial hybrids,” *New J. Phys.* **13**, 093034 (2011).
- C. Navau, J. Prat-Camps, and A. Sanchez, “Magnetic energy harvesting and concentration at a distance by transformation optics,” *Phys. Rev. Lett.* **109**, 263903 (2012).
- J. Prat-Camps, C. Navau, and A. Sanchez, “Experimental realization of magnetic energy concentration and transmission at a distance by metamaterials,” *Appl. Phys. Lett.* **105**, 234101 (2014).
- C. Navau, R. Mach-Battle, A. Parra, J. Prat-Camps, S. Laut, N. Del-Valle, and A. Sanchez, “Enhancing the sensitivity of magnetic sensors by 3D metamaterial shells,” *Sci. Rep.* **7**, 44762–44769 (2017).
- B. Kibret, M. Premaratne, P. M. Lewis, R. Thomson, and P. B. Fitzgerald, “A time-varying magnetic flux concentrator,” *J. Phys. D: Appl. Phys.* **49**, 335003 (2016).
- E. Fourneau, J. A. Arregi, A. Barrera, N. D. Nguyen, S. Bending, A. Sanchez, V. Uhlir, A. Palau, and A. V. Silhanek, “Microscale metasurfaces for on-chip magnetic flux concentration,” *Adv. Mater. Technol.* **8**, 2300177 (2023).
- J. Prat-Camps, A. Sanchez, and C. Navau, “Superconductor–ferromagnetic metamaterials for magnetic cloaking and concentration,” *Supercond. Sci. Technol.* **26**, 074001 (2013).
- V. Moshchalkov, J. Henry, C. Marin, J. Rossat-Mignod, and J. Jacquot, “Anisotropy of the first critical field and critical current in YBa<sub>2</sub>Cu<sub>3</sub>O<sub>6.9</sub> single crystals,” *Physica C* **175**, 407–418 (1991).
- L. Krusin-Elbaum, A. P. Malozemoff, Y. Yeshurun, D. C. Cronmeyer, and F. Holtzberg, “Temperature dependence of lower critical fields in Y-Ba-Cu-O crystals,” *Phys. Rev. B* **39**, 2936–2939 (1989).
- S. Voltan, C. Cirillo, H. J. Snijders, K. Lahabi, A. García-Santiago, J. M. Hernández, C. Attanasio, and J. Aarts, “Emergence of the stripe-domain phase in patterned permalloy films,” *Phys. Rev. B* **94**, 094406 (2016).
- S. Singh, H. Gao, and U. Hartmann, “Nucleation of stripe domains in thin ferromagnetic films,” *Phys. Rev. B* **98**, 060414 (2018).
- G. Shaw, J. Brisbois, L. B. G. L. Pinheiro, J. Müller, S. Blanco Alvarez, T. Devillers, N. M. Dempsey, J. E. Scheerder, J. Van de Vondel, S. Melinte, P. Vanderbenden, M. Motta, W. A. Ortiz, K. Hasselbach, R. B. G. Kramer, and A. V. Silhanek, “Quantitative magneto-optical investigation of superconductor/ferromagnet hybrid structures,” *Rev. Sci. Instrum.* **89**, 023705 (2018).
- C. Luo, Y. Fu, D. Zhang, S. Yuan, Y. Zhai, S. Dong, and H. Zhai, “Temperature dependent coercivity and magnetization of light rare-earth Nd doped permalloy thin films,” *J. Magn. Magn. Mater.* **374**, 711–715 (2015).
- Y. Zhao, Q. Song, S.-H. Yang, T. Su, W. Yuan, S. S. P. Parkin, J. Shi, and W. Han, “Experimental investigation of temperature-dependent Gilbert damping in permalloy thin films,” *Sci. Rep.* **6**, 22890 (2016).
- I. Soldatov and R. Schäfer, “Selective sensitivity in Kerr microscopy,” *Rev. Sci. Instrum.* **88**, 073701 (2017).
- D. Stamopoulos, N. Moutis, M. Pissas, and D. Niarchos, “Effective ferromagnetic coupling between a superconductor and a ferromagnet in La Ca Mn O/Nb hybrids,” *Phys. Rev. B* **72**, 212514 (2005).
- D. Stamopoulos, E. Manios, and M. Pissas, “Synergy of exchange bias with superconductivity in ferromagnetic–superconducting layered hybrids: The influence of in-plane and out-of-plane magnetic order on superconductivity,” *Supercond. Sci. Technol.* **20**, 1205 (2007).
- E. Aristomenopoulou and D. Stamopoulos, “Superconducting magnetoresistance effect observed in Co/Nb/Co trilayers under a parallel magnetic field: The importance of matching the width of magnetic domain walls of the Co layers with the thickness of the Nb interlayer,” *J. Appl. Phys.* **118**, 063904 (2015).
- A. Y. Aladyshkin, A. V. Silhanek, W. Gillijns, and V. V. Moshchalkov, “Nucleation of superconductivity and vortex matter in superconductor–ferromagnet hybrids,” *Supercond. Sci. Technol.* **22**, 053001 (2009).